

## Article

# Simulation, Set-Up, and Thermal Characterization of a Water-Cooled Li-Ion Battery System

Max Feinauer <sup>1</sup>, Nils Uhlmann <sup>2</sup>, Carlos Ziebert <sup>2</sup> and Thomas Blank <sup>1,\*</sup>

<sup>1</sup> Institute for Data Processing and Electronics (IPE), Karlsruhe Institute of Technology (KIT), Hermann-von-Helmholtz-Platz 1, 76344 Eggenstein-Leopoldshafen, Germany

<sup>2</sup> Institute for Applied Materials (IAM)—Applied Materials Institute of Technology (KIT), Hermann-von-Helmholtz-Platz 1, 76344 Eggenstein-Leopoldshafen, Germany

\* Correspondence: thomas.blank@kit.edu

**Abstract:** A constant and homogenous temperature control of Li-ion batteries is essential for a good performance, a safe operation, and a low aging rate. Especially when operating a battery with high loads in dense battery systems, a cooling system is required to keep the cell in a controlled temperature range. Therefore, an existing battery module is set up with a water-based liquid cooling system with aluminum cooling plates. A finite-element simulation is used to optimize the design and arrangement of the cooling plates regarding power consumption, cooling efficiency, and temperature homogeneity. The heat generation of an operating Li-ion battery is described by the lumped battery model, which is integrated into COMSOL Multiphysics. As the results show, a small set of non-destructively determined parameters of the lumped battery model is sufficient to estimate heat generation. The simulated temperature distribution within the battery pack confirmed adequate cooling and good temperature homogeneity as measured by an integrated temperature sensor array. Furthermore, the simulation reveals sufficient cooling of the batteries by using only one cooling plate per two pouch cells while continuously discharging at up to 3 C.

**Keywords:** Li-ion battery pack; water-cooled battery system; cooling plate; lumped battery model; temperature measurement



**Citation:** Feinauer, M.; Uhlmann, N.; Ziebert, C.; Blank, T. Simulation, Set-Up, and Thermal Characterization of a Water-Cooled Li-Ion Battery System. *Batteries* **2022**, *8*, 177. <https://doi.org/10.3390/batteries8100177>

Academic Editors: Matthieu Dubarry and Michael Danzer

Received: 26 July 2022

Accepted: 8 October 2022

Published: 12 October 2022

**Publisher's Note:** MDPI stays neutral with regard to jurisdictional claims in published maps and institutional affiliations.



**Copyright:** © 2022 by the authors. Licensee MDPI, Basel, Switzerland. This article is an open access article distributed under the terms and conditions of the Creative Commons Attribution (CC BY) license (<https://creativecommons.org/licenses/by/4.0/>).

## 1. Introduction

A high energy and power density, a high efficiency, and a long cycle lifetime make Li-ion batteries the predominating electrochemical energy storage for various applications. The ongoing research on new materials for Li-ion batteries is continuously improving these properties. In recent years, an increasing amount of graphite could be replaced by Si in the anode by suppressing large volume changes while benefiting from the much higher specific capacity of pure Si [1,2]. On the cathode side, especially, higher energy contents are realized by increasing the Ni content to more than 80% in mixtures with Mn and Co (NMC) or Co and Al (NCA) in layered transition metal oxides [3,4]. Simultaneously, cathode materials, such as  $\text{LiMn}_x\text{Fe}_{1-x}\text{PO}_4$  (LMFP) are developed, combining high safety and slow degradation of  $\text{LiFePO}_4$  (LFP) and high specific energy of  $\text{LiMnPO}_4$  [5].

Depending on the application and the associated requirements, different materials are favored. For automotive and stationary applications, a long cycle life and high safety are the most important requirements [6,7]. Apart from the wide range of ambient temperatures, high charging rates are the main challenges for automotive applications, e.g., in electrical vehicles [8]. A well-known application of stationary battery systems is stabilizing the electric grid for compensating weather-related fluctuations of wind or solar power [9]. Stationary energy storage systems based on second-life applications of Li-ion batteries previously used in mobile applications could help to reduce the cost of expensive Li-ion batteries and save valuable lithium reserves [10–13]. Depending on the first-life aging conditions, the safety properties can be drastically decreased, demanding careful treatment [14].

A strict voltage and temperature range must be maintained to ensure the safe and efficient operation of a Li-ion battery with slow performance degradation [15,16]. Additional factors, such as cell chemistry or charge and discharge rates, can greatly influence battery degradation and safety behavior [17–19]. A typical cycle lifetime is in the range of 2000 cycles for gentle battery operation [20]. The capacity fade of a battery induced by different aging mechanisms is quantified by the state of health (SOH). It is defined by the quotient of the current battery capacity after a certain number of charge/discharge cycles and the battery capacity of the first cycle. Several factors, such as limiting the cycling voltage range to a narrow window at a medium state of charge (SOC), can significantly increase the battery lifetime [21].

Moreover, for typical Li-ion batteries, operating temperatures of approximately 25 °C lead to the lowest aging rate [22]. As schematically shown in Figure 1, the capacity fade increases with temperature due to an accelerated growth of the solid electrolyte interface (SEI) [22]. Hence, a typical end-of-life criterion of 80% SOH is reached much faster. As experimental data from Waldmann et al. (cylindrical cells with graphite anode and  $\text{Li}_x\text{Ni}_{1/3}\text{Mn}_{1/3}\text{Co}_{1/3}\text{O}_2/\text{Li}_y\text{Mn}_2\text{O}_4$  cathode) show, the capacity fade increased by more than 25% at 50 °C and almost twice as high at 60 °C compared to 25 °C [22]. At temperatures typically below 25 °C, Li plating becomes favorable, also leading to strong capacity fading and lowered battery safety [14]. The exact optimum temperature of a Li-ion battery depends on multiple factors, such as cell chemistry and cell type (i.e., cylindrical cell, pouch cell, or prismatic cell), electrode thickness, and cycling rate [18,23]. While slight deviations from the optimum temperature are tolerable, more significant variations must be prevented [24].

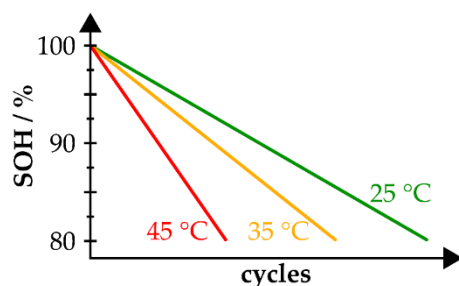


**Figure 1.** Simplified capacity fade of a typical Li-ion battery vs. number of cycles for different operating temperatures.

Different additives for the liquid electrolyte can improve the performance and thermal stability of Li-ion batteries at elevated temperatures [25]. Additives, such as vinylene carbonate (VC), trimethylene sulfone (TMS), propane sulfone (PS), and many others affect the SEI in such a way that it either creates a thinner or more robust film [26–29]. Nevertheless, such electrolyte additives can have undesired side effects, such as reduced performance at low temperatures [26]. A totally different approach under current research is the shielding of the electrolyte inside silicide nanowires as anode material to prohibit the formation of an SEI, leading to excellent cycle lives even at high loads [30].

The most common way to improve the battery cycle life by adjusting the temperature to an optimum is by adding a thermal management system to the battery pack. Even if the average battery temperature has greater relevance concerning battery aging than temperature gradients [31], active tempering can help to reduce natural temperature gradients within an operated battery and between different batteries in a pack. An inhomogeneous temperature distribution leads to irregular degradation and unbalancing, resulting in a reduced battery pack performance [32,33]. Typically, a maximum allowed temperature gradient over the battery of 5 K is defined [34].

For many applications, such as stationary energy storage systems at comfortable ambient temperatures, a battery thermal management system only needs to remove the heat generated while operating. Hence, the thermal management system can be equated

with a cooling system. Other than standard operation cooling, the cooling system should suppress overheating in case of a battery failure and thereby prohibit propagation to other cells by an efficient emergency cooling [35]. Especially due to the safety concerns, the additional costs for a thermal management system are indispensable. An extended lifetime of optimally tempered batteries further puts the costs for a thermal management system into perspective and is a simple approach to more sustainability.

With the increased usage of Li-ion batteries, especially in the last two decades, different safety and cooling systems have been developed or adapted to battery systems. The four most common cooling systems listed with increasing complexity and cooling efficiency are passive fin cooling, forced air cooling, and direct and indirect liquid cooling [36]. Especially in densely packed battery packs operated with high loads, liquid cooling systems are more efficient than air cooling systems, i.e., they have a lower parasitic power consumption [32]. In addition to these cooling systems, alternatives based on heat pipes [37,38], boiling cooling [39], or phase change materials [40–42] have been investigated.

Different approaches optimizing the design of cooling plates concerning competing factors, such as parasitic power consumption, size, weight, cooling efficiency, and temperature homogeneity, have been created by simulations [43–47]. This work developed an optimized cooling plate design based on these previous works. A fluid flow simulation of the cooling plate is combined with a thermal simulation of the battery to size and further optimize the system. The modular design of the battery system components starting at the cell level enables an easy adaptation to different applications and upscaling to larger systems. The cooling plates can also be used as heating plates, which is especially necessary for automotive applications in cold ambient temperatures at the start. Hence, the spectrum of possible applications of the cooling plates is enlarged and correlated with a high industrial interest (see patents [48–51]).

A well-established and high-performing model to describe a Li-ion battery is based on the porous electrode theory [52] and was later expanded by Doyle and Newman [53]. The crux of this model is the required detailed knowledge of the internal battery structure and material properties, which are in practice often unknown and great efforts must be put into determining them. Therefore, the simplified lumped battery model homogenizes the whole battery cell. Hence, only a small set of parameters is needed to model the battery, which thermal and electrical measurements can non-destructively determine. Even if the lumped battery model cannot describe the inhomogeneous heating of the cell itself, it can consider the actual temperature distribution over the battery, which can change while operating. This is especially important because the total heat generation is strongly influenced by temperature [54].

Based on the simulative results, aluminum cooling plates were manufactured and integrated into a previously developed battery module. For the experimental validation of the simulation and, with it, the functionality of the cooling system, an integrated temperature sensor array with associated measurement electronic is developed. By measuring the temperature distribution within an operated battery pack with this sensor array, also errors in the setup can be disclosed. Finally, an extended evaluation of the water-cooled battery system can be performed by comparing experimental and simulative results.

## 2. Simulative Methods

The simulation of the battery pack is divided into two parts. First, the battery is electrochemically modeled to further calculate the heating rate. Based on the heat dissipation of the batteries, the necessary cooling power can be determined. Secondly, a fluid flow simulation of the cooling unit improves cooling efficiency and temperature distribution.

### 2.1. The Lumped Battery Model

The lumped battery model, used for electrochemical and thermal modeling of the Li-ion battery, is fully implemented in COMSOL Multiphysics. The generated heat is calculated as a function of battery temperature, SOC, and applied current. Therefore, a

reduced set of parameters, including battery capacity, open-circuit-voltage (OCV) curve at a reference temperature, its temperature derivation, and voltage losses due to Ohmic resistance, charge transfer, and diffusion, are needed. These parameters can be directly or indirectly determined by a nondestructive, electrochemical characterization of the battery.

The temperature-dependent OCV over SOC-curve can be determined with the OCV-curve at reference temperature  $T_{\text{ref}}$  and the linear temperature derivation is given by:

$$U_{\text{OCV}}(T, \text{SOC}) = U_{\text{OCV}}(T_{\text{ref}}, \text{SOC}) + (T - T_{\text{ref}}) \cdot \frac{dU_{\text{OCV}}(T, \text{SOC})}{dT}. \quad (1)$$

This theoretic cell potential is always related to a thermodynamic equilibrium. As soon as a current  $I$  flows through the battery, a nonequilibrium is reached resulting in a deviation of the actual cell potential  $U_{\text{cell}}$  from the equilibrium potential  $U_{\text{OCV}}$ . The overpotential  $\eta$  can be expressed as:

$$\eta = U_{\text{cell}} - U_{\text{OCV}} = \eta_{\text{Ohm}} + \eta_{\text{act}} + \eta_{\text{conc}}. \quad (2)$$

This shows the single contributions to the overpotential due to the Ohmic overpotential  $\eta_{\text{Ohm}}$ , the activation overpotential  $\eta_{\text{act}}$ , and concentration overpotential  $\eta_{\text{conc}}$ . The Ohmic overpotential is related to the internal resistance  $R_i$  by:

$$\eta_{\text{Ohm}} = R_i \cdot I = \eta_{\text{Ohm},1\text{C}} \cdot \frac{I}{I_{1\text{C}}}. \quad (3)$$

For generalization, one typically uses the Ohmic overpotential  $\eta_{\text{Ohm},1\text{C}}$ , which is normalized to a current of 1 C.

The activation overpotential as a function of the current follows from the Butler–Volmer equation at temperature  $T$  with Faraday's constant  $F$  and gas constant  $R$ . For Li-ion batteries, the number of involved electrons is  $z = 1$ . Considering the symmetry of anode and cathode, the dimensionless charge transfer factor in the Butler–Volmer equation can be set to  $\alpha_a = \alpha_c = 1/2$  for anode and cathode, where  $\alpha_a + \alpha_c = 1$  is satisfied. The simplified equation, solved for the activation overpotential, is then given by [55]:

$$\eta_{\text{act}} = \frac{2RT}{F} \cdot \text{arsinh}\left(\frac{I}{2J_0 I_{1\text{C}}}\right). \quad (4)$$

$J_0$  is a dimensionless exchange current.

The concentration overpotential results from finite transport rates into the particles, described by a particle-diffusion model. The corresponding time constant  $\tau$  determines the relaxation time of the battery to return to the OCV. The relaxation time strongly depends on the amount of the previously applied current. A more detailed description is given by Ekström et al. [55].

Further effects influencing the cell voltage, such as a current-dependent hysteresis of the OCV curve or aging effects, are not further considered to keep the model's simplicity.

The most comfortable way to determine the dedicated parameters of the overpotentials  $\eta_{\text{Ohm},1\text{C}}$ ,  $J_0$ , and  $\tau$  is fitting a dynamic load curve defined by an applied current with the lumped battery model. Therefore, an optimization algorithm in COMSOL is used for continuously varying the parameters. The algorithm thereby minimizes the difference between measured and calculated voltage as a function of the applied current.

Knowing these parameters and the overpotentials allows us to calculate the battery voltage with Equation (2). Furthermore, the voltage drop, due to the Ohmic and activation overpotential is directly connected with the irreversibly generated heat of the battery by the current. An additional contribution to the irreversible heat generation is given by the mixing heat  $\dot{Q}_{\text{mix}}$ . The mixing heat is directly related to the concentration overpotential

taking local SOC distributions into account. Further considering the contribution of the reversible heat  $\dot{Q}_{\text{rev}}$ , the heat generation  $\dot{Q}$  of the battery can be calculated by [56]:

$$\dot{Q} = \dot{Q}_{\text{ohm}} + \dot{Q}_{\text{act}} + \dot{Q}_{\text{mix}} + \dot{Q}_{\text{rev}} = (\eta_{\text{ohm}} + \eta_{\text{act}}) \cdot I + \dot{Q}_{\text{mix}} - T \cdot I \cdot \frac{dU_{\text{OCV}}}{dT}. \quad (5)$$

If this amount of heat cannot be removed from the battery, the battery heats up. The temperature rise depends thereby on the batteries heat capacity.

## 2.2. Water-Cooled Battery System

The lumped battery model is extended to three dimensions for the water-cooled battery system simulation. Furthermore, a heat transfer and nonisothermal fluid flow finite-element simulation are added to the system model. Therefore, different heat conductivities for all directions are considered. The heat generation is calculated for each volume element of the battery within the finite-element simulation, taking the local temperature into account.

The ideal cooling power  $\dot{Q}$  of an active cooling system can be determined by:

$$\dot{Q} = c_p \dot{m} \Delta T = \rho c_p \dot{V} \Delta T. \quad (6)$$

Hence, in a cooling fluid with heat capacity  $c_p$ , and mass density  $\rho$ , the cooling power depends on mass flow rate  $\dot{m}$  or volume  $\dot{V}$  flow rate, and the temperature difference  $\Delta T$  between fluid inlet and outlet. For a given heat output that needs to be removed, the temperature difference and the temperature gradient within the battery can be set up by the volume flow rate. Minimum temperature gradients over the battery require a high flow rate resulting in a trade-off between the cooling system requirements and parasitic power consumption. The pumping power  $P$  linearly increases with volume flow rate by:

$$P = \Delta p \cdot \dot{V}. \quad (7)$$

The pressure drop  $\Delta p$  is defined by the pressure difference from the fluid inlet to the fluid outlet within the considered system.

Since the expected flow rates are comparably low, a laminar stream is sufficient for describing the stream. The examination of the velocity distribution of the fluid in the cooling plate is a simple way to evaluate the temperature distribution. The fluid stream must be consistent in all parts of the cooling plate for a uniform temperature distribution. Therefore, the cooling plate's internal structure is modified so that all parts and subchannels are equally streamed. An optimized design can be found by evaluating the stream velocity or temperature distribution's standard deviation.

## 3. Experimental Battery Characterization

For a precise simulation of the battery system, different properties, including electrical and thermal characteristics of the batteries, must be known. Therefore, a pouch cell used to build up the battery system is characterized. The pouch cell (Litacell LC-44 from LITARION) has a NMC cathode and a graphite anode. Its nominal capacity is 44 Ah within a voltage range of (3.0–4.2) V. The battery weighs 990 g and has dimensions of 155 mm × 249 mm × 12 mm (width × height × thickness).

### 3.1. Electrochemical Characterization

The electrochemical characterization of the pouch cell is performed with a bidirectional power supply SM500-CP-90 (DELTA Electronika) used for charging and discharging. A LabVIEW program is used to control the power supply and data tracking.

To determine the OCV curve with minimal hysteresis influence, the battery is charged and discharged with short current pulses [57]. Each pulse has a duration of 144 s and, therefore, a SOC-variation of a maximum of 2% if the current is limited to a rate of  $C/2$  and

voltage to the specified voltage range. The rest time between two pulses was chosen to be one hour, sufficient to almost complete the relaxation period [58].

Moreover, a load profile defined by a current with different current steps, step times, and relaxation times is applied to the battery. Thereby, the voltage of the battery is measured. The load profile with a total time of 1300 s and step times between 1 s and 12 s dynamically varies within a current range of  $\pm 1$  C ( $\pm 44$  A). The same load profile is used as input to the optimization study of the lumped battery model. Therewith, the key parameters of the overpotentials were determined to be  $\eta_{\text{Ohm},1\text{C}} = 0.0231$  V,  $J_0 = 0.6361$ , and  $\tau = 1276.9$  s. The standard deviation for the optimization of the voltage is 5.5 mV. A significant factor contributing to this deviation is the sampling interval of 250 ms, especially in fast-changing current profiles being too slow to detect fast voltage changes.

The temperature derivation of the OCV-curve is determined at several SOC values. Therefore, a fully discharged battery at the reference temperature of 25 °C is charged until the desired SOC with a subsequent relaxation phase of 4 h. Afterward, the battery is electrically disconnected and cooled down to 5 °C in a climate chamber. The voltage is measured when the temperature reaches a steady state, and the temperature is increased by 10 K in the next step. This procedure of thermal relaxation, voltage measurement, and further temperature increase is repeated up to a temperature of 45 °C. Next, the battery is charged to a new SOC, and the whole procedure is repeated. The decreasing trend of the voltage with increasing temperature can be seen in Figure 2a for different SOC values. To better compare different voltages at various SOC, the voltages are related to their value at the lower temperature limit.

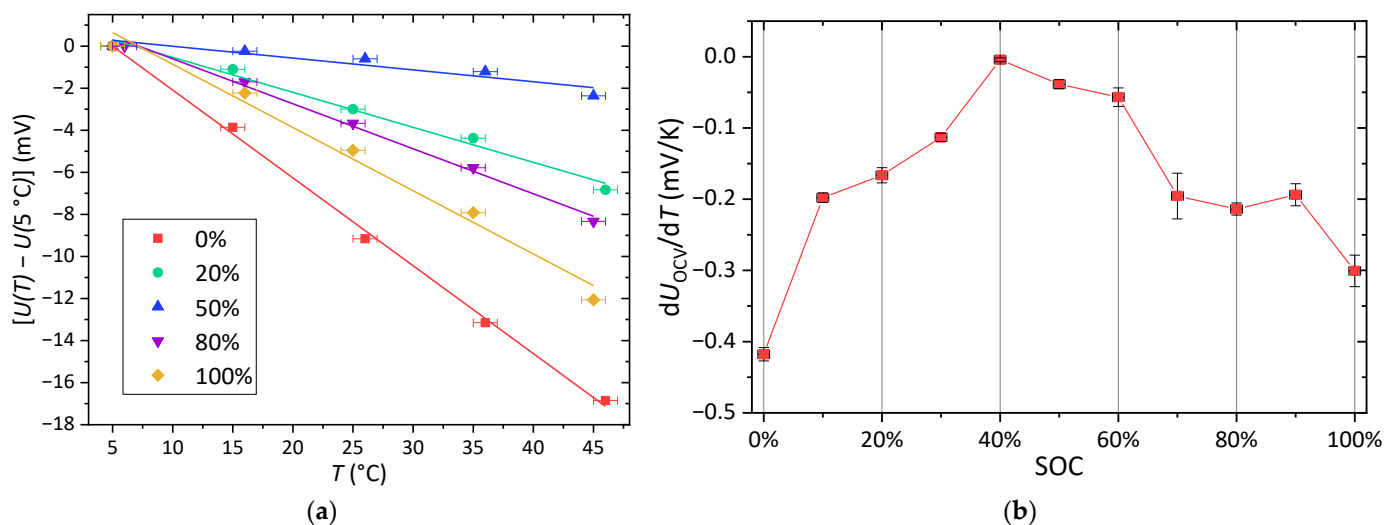


**Figure 2.** SOC-dependent voltage variation with temperature: (a) battery voltage as a function of temperature related to the voltage at  $T \approx 5$  °C for selected SOC values with corresponding linear fits. (b) Slopes of the linearized voltage variation with temperature depending on the SOC. A line is drawn to guide the eye.

Plett [59] states a linear relationship between voltage and temperature. This is verified for the considered temperature range by the data points shown in Figure 2a. Therefore, the data points are fitted linearly. The slopes of these fits are plotted versus SOC in Figure 2b. This curve is characteristic of each battery type [59]. Interestingly, the temperature derivation of the voltage is for all SOC negative. Most curves in the literature show a similar SOC dependence but with an offset leading to positive voltage variations with temperature in the medium SOC range [59–61]. Since  $dU/dT$  is directly related to the reversible heat generation while cycling the battery, the result could be confirmed by comparing the generated heat while charging and discharging.

### 3.2. Thermal Characterization

The transversal thermal conductivity is the main limiting factor for cooling the pouch cells at the plane sides. Therefore, the cooled battery simulation demands a precise knowledge of the transversal thermal conductivity. For the lateral thermal conductivity, a literature value of 35 W/mK is further used [62,63]. Anyway, for an improved description of the in-plane temperature nonuniformity, all layers of the pouch cell should be measured separately [64], which does not satisfy the simple model in this work.

By applying Fourier's law, the transversal thermal conductivity of the pouch cell is determined. As shown in Figure 3, the pouch cell and reference material are placed between a cooling and a heating plate, providing a constant temperature of approx. 20 °C and 70 °C, respectively. If the reference material and pouch cell areas are the same, the heat flow from warm to cold plate is conserved. A heat-conducting foil is placed between the layers in the setup to obtain good thermal contact. For a thermal conductivity of the reference material  $\lambda_{\text{ref}}$  with thickness  $d_{\text{ref}}$ , the heat flux could be calculated by the temperature difference  $\Delta T_{\text{ref}} = T_4 - T_3$  between the upper and lower side. Further measuring of the temperature difference  $\Delta T = T_2 - T_1$  through the pouch cell of thickness  $d$ , the transversal thermal conductivity  $\lambda$  can be determined in equilibrium state by:

$$\lambda = \lambda_{\text{ref}} \cdot \frac{\Delta T_{\text{ref}}}{d_{\text{ref}}} \cdot \frac{d}{\Delta T} \quad (8)$$

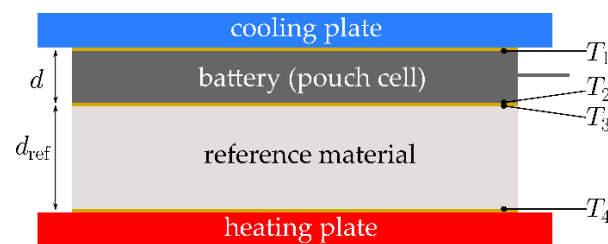


**Figure 3.** Experimental setup to determine the transversal thermal conductivity of a pouch cell under application of Fourier's law. Temperatures are measured at positions 1–4.

The determined transversal thermal conductivity of the Litarion pouch cells is  $(1.89 \pm 0.07)$  W/mK. Maleki et al. determined slightly smaller values for different pouch cells in the range of (1.19–1.63) W/mK by the xenon flash technique [63].

The effective specific heat capacity of the cell was determined in an EV accelerating rate calorimeter (ARC) from Thermal Hazard Technology combined with a power-controlled heater foil. As shown in the schematic drawing in Figure 4, the calorimeter chamber with a diameter of 25 cm and a height of 50 cm has one heater and one thermocouple located in the lid and bottom, and two heaters and thermocouples (all type N) in the sidewall.

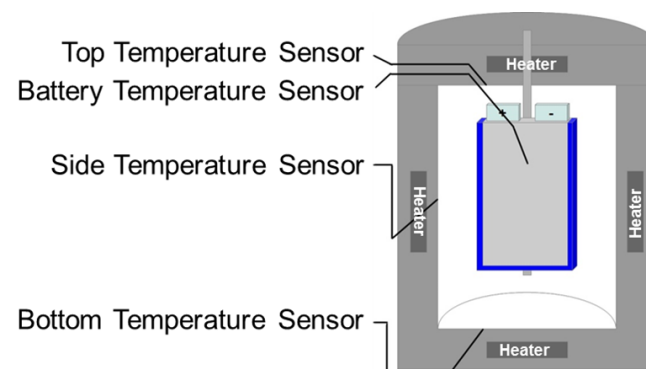


**Figure 4.** Schematic drawing of an accelerating rate calorimeter with a pouch cell in the cylindrical chamber.

The heaters work until they reach the required temperatures, depending on the measurement conditions and modes. Another type N thermocouple is attached to the middle of the front surface of the cell, which is the primary or so-called bomb thermocouple that controls the calorimeter temperature. Here, the adiabatic mode is used. In this mode, the heaters immediately follow any increase in the surface temperature of the cell, thus, the cell cannot transfer heat to the surrounding walls. By applying a certain current and voltage to the foil over a defined period  $[t_1, t_2]$ , the total supplied heat

$$\Delta Q = \int_{t_1}^{t_2} U \cdot I \, dt \quad (9)$$

is known.

A “sandwich” layout (Figure 5) was used, where the heater foil (an area smaller than the cell surface area) was placed tightly between two cells so that all heat generated by the foil is transferred by conduction to the two cells. The maximum current and voltage applied to the heater foil are adjusted to achieve a constant heating rate of ca. 0.3 K/min.

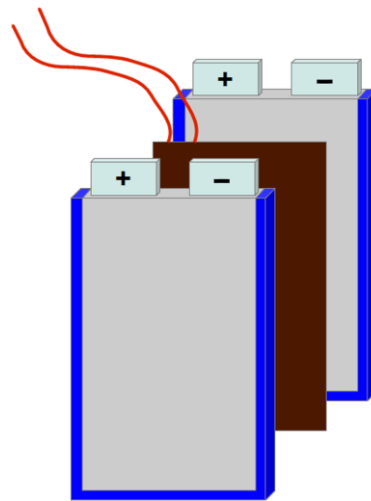


**Figure 5.** Sandwich setup used inside the EV ARC for the heat capacity determination. A heater foil is placed between two pouch cells.

The temperature change of the two cells under adiabatic conditions,  $\Delta T_{\text{ad}}$ , was measured in the ARC and the corresponding heat transferred from the heater foil to the cells is:

$$\Delta Q = c_p \cdot m \cdot \Delta T_{\text{ad}}. \quad (10)$$

From this equation, using the known mass  $m$  of the cell, the heat capacity can be determined as a function of temperature in the range between 28 °C and 60 °C by:

$$c_p = \frac{\Delta Q}{m \cdot \Delta T_{\text{ad}}} = \frac{\int_{t_1}^{t_2} U \cdot I \, dt}{m \cdot \Delta T_{\text{ad}}}. \quad (11)$$

The average results from four measurements are shown in Figure 6. It can be seen that the specific heat capacity increases from 1.15 kJ/(kgK) to 1.33 kJ/(kgK) in that temperature range.

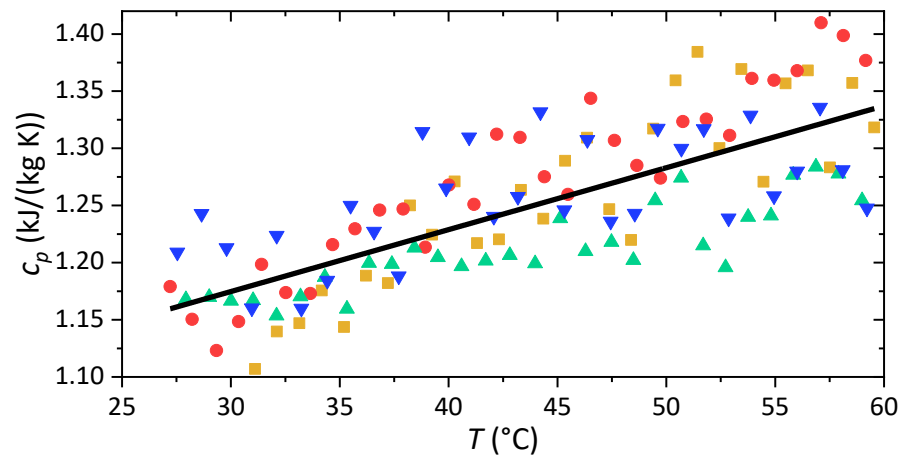


**Figure 6.** Specific heat capacity as a function of temperature in the range between 28 °C and 60 °C from four measurements (different symbols) with linear fit (black line).

#### 4. Simulative Results

##### 4.1. Electrochemical and Thermal Behavior of a Single Battery

With the previously determined electrochemical parameters of the battery, the electrochemical and thermal model of the battery can be set up. For a better understanding of the total heat generation of the battery, the single heat contributions are discussed first.

The single contributions to the heat generation are shown in Figure 7a for charging and discharging the battery at 1 C. Note that the heat generation due to the Ohmic and activation overpotential is independent of SOC, only depending on the amount of the current. It is therefore, equal to charging and discharging. The substantial increase in the mixing heat at the end of charging and especially at the end of discharging reveals the limitations of the lumped battery model. Due to finite diffusion time constants  $\tau$ , the SOC at the particle surface is already zero in case of discharging. At the same time, the average SOC is still more significant than zero leading to theoretically negative SOC and vice versa for charging. As the definition of the reversible heat contribution states, the generated heat is just the opposite for charging and discharging. The SOC dependency is due to Equation (5), governed by the temperature derivation of the voltage shown in Figure 2b. Especially when operating the battery at low current rates, the contribution of reversible heat generation can even exceed the contribution of irreversible heat generation [65].

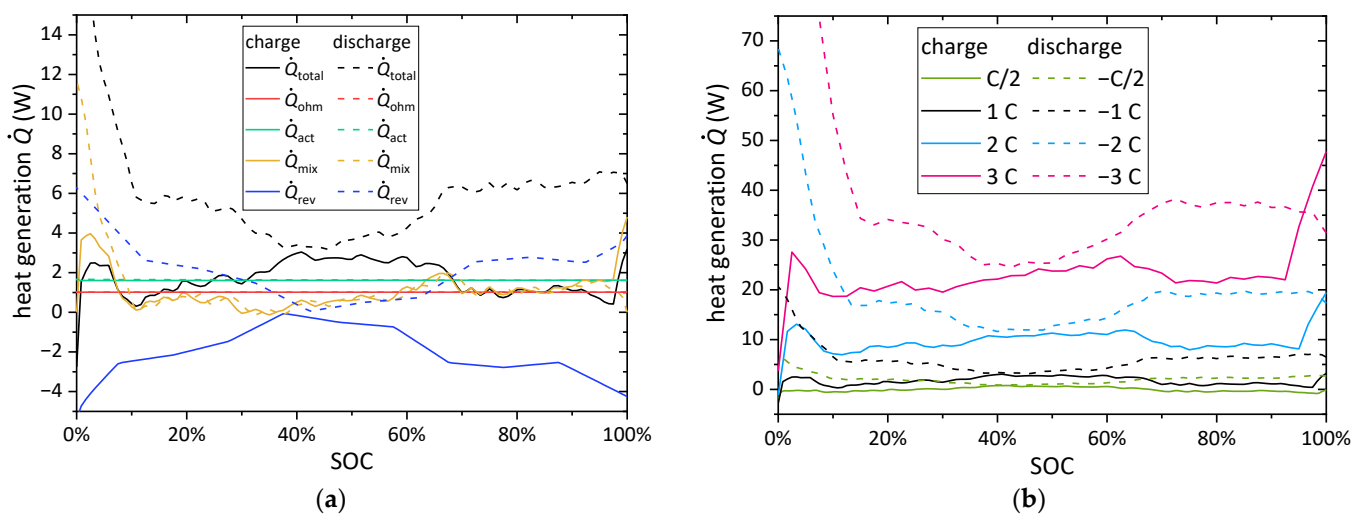


**Figure 7.** Heat generation of a pouch cell calculated with the lumped battery model as a function of the SOC. (a) Single contributions to the heat power for charging (solid lines) and discharging (dashed lines) with 1 C. (b) Total heat generation for different C-rates for charging and discharging.

In addition to the dependency of the heat generation from SOC and relaxation state in highly dynamic loads, the applied current has the greatest influence on the amount of generated heat. Therefore, the heat generation is calculated for continuous charging and discharging at different current rates ( $C/2$ ,  $1 C$ ,  $2 C$ , and  $3 C$ ). As shown in Figure 7b, the generated heat increases dramatically with C-rate due to a non-linear current dependency of the overpotentials. The enormously increased concentration overpotential for higher applied currents leads to the previously mentioned modeling problems for a negative particle surface SOC at earlier stages.

Considering the temperature dependent heat capacity of the battery, in an adiabatic system, the battery temperature would be raised approximately 18.6 K and 26.7 K after discharging with  $1 C$  and  $2 C$ , respectively. Further considering that the discharge time at a rate of  $2 C$  is only half that for  $1 C$ , illustrates once more the necessity for cooling batteries operated with high loads.

#### 4.2. Thermal Behavior of a Water-Cooled Battery Pack

Based on a known, especially current dependent battery heat generation, the cooling system could now be designed considering the critical parameters of cooling efficiency, cooling homogeneity, and system pressure drop. Therefore, different designs and design parameters of cooling plates were evaluated.

Excellent thermal coupling of the batteries to the coolant flow is ensured by choosing aluminum for the cooling plates. Hence, as the finite-element simulation shows, the cooling efficiency is quite suitable for all cooling plate designs.

A design based on parallel fluid channels is favored in the tradeoff between a homogenous flow through the cooling plate and a low pressure drop. A meander-shaped cooling channel design provides a similar temperature distribution but correlates with a higher pressure drop and, therefore, is less preferable. A vertical shift of the walls inside the cooling plate separating the single channels improves the fluid flow by equalizing the flow rate through each channel.

As the simulated velocity distribution in Figure 8a reveals, for a low flow rate of  $0.1 \text{ L/min}$ , all fluid channels in the improved parallel design have almost the same stream velocity. Therefore, a homogenous cooling in all parts of the cooling plate is secured. In the case of high flow rates (e.g.,  $1.0 \text{ L/min}$  in Figure 8b), the channels' flow was inconsistent. This inconsistent velocity distribution is directly coupled to the non-homogenous temperature distribution in Figure 8c on top of the cooling plate after discharging at  $3 C$ . Especially in the lower-left corner, insufficient cooling was obtained. However, considering the absolute temperature difference of less than  $2 \text{ K}$  over the cooling plate, these cooling plates are suitable even for high flow rates in combination with high cooling requirements.

A homogenous temperature distribution of the cooling plate is an essential requirement for a homogenous battery temperature distribution. To complete the water-cooled battery model, batteries are added in the next step. For simplicity, one unit of two batteries and one cooling plate is further considered instead of the whole battery pack.

At medium loads of the batteries, such as discharging with  $1 C$ , a low flow rate of  $0.1 \text{ L/min}$  through the cooling plates is sufficient to obtain excellent and homogenous cooling. This is shown by the simulated temperature distribution in Figure 9a, where the maximum temperature difference over the battery is less than  $1 \text{ K}$ .

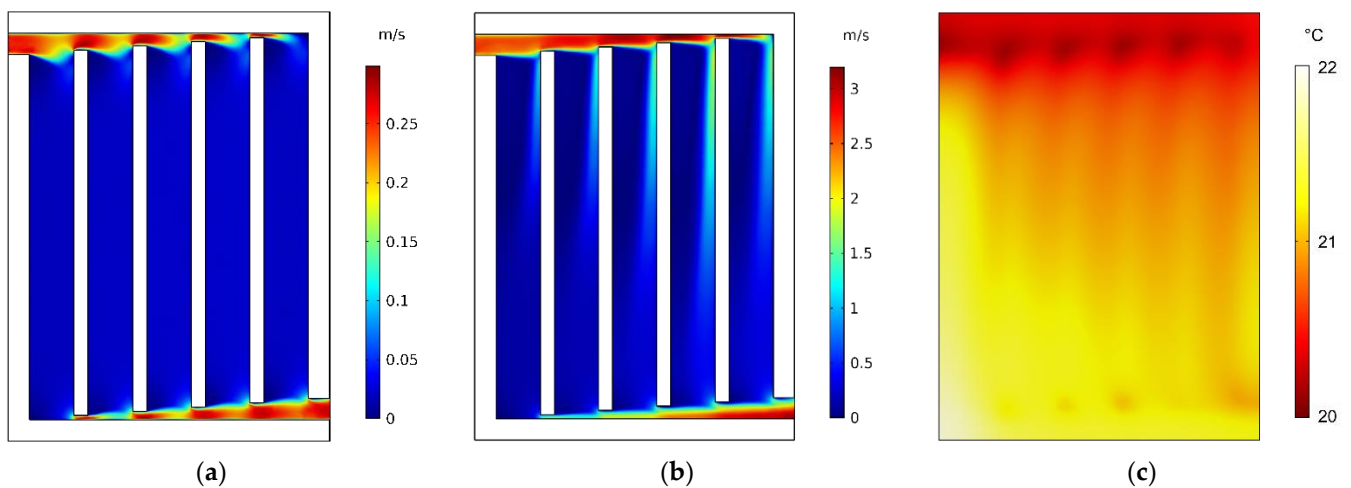


**Figure 8.** Simulation of velocity and temperature distribution of a cooling plate (fluid inlet at top left and outlet at bottom right): (a) velocity distribution for a low flow rate of 0.1 L/min, (b) velocity distribution for a high flow rate of 1 L/min, and (c) temperature distribution for 1 L/min and 20 °C water inlet temperature after discharging with 3 C.

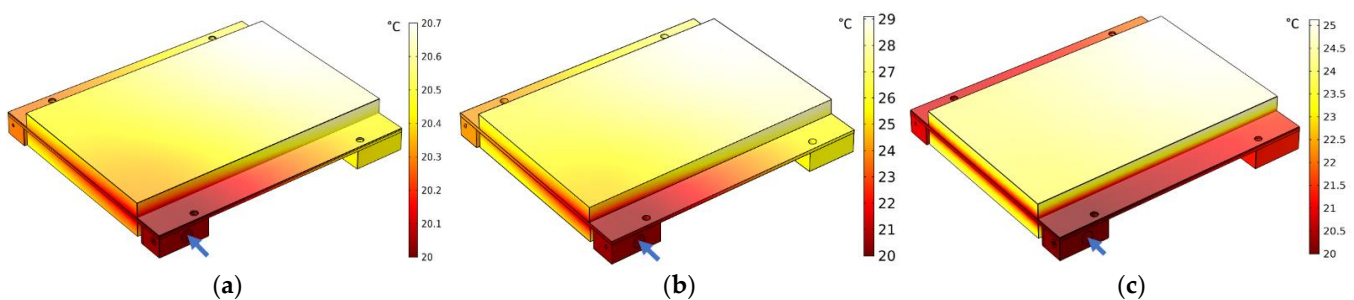


**Figure 9.** Simulated heat distribution in a unit of two pouch cells (rectangular block on top and bottom) and one cooling plate. Through the inlet (blue arrow) flows water into the cooling plate at an ambient temperature of 20 °C. (a) After discharging with 1 C and flow rate of 0.1 L/min and after discharging with 3 C at flow rate of (b) 0.1 L/min and (c) 0.5 L/min.

The simulated temperature distribution of the cooling system for a high load (discharging with 3 C) with same flow rate of 0.1 L/min is shown in Figure 9b. There, a maximum temperature rise of 9 K over the battery is obtained, highlighting an insufficient cooling. As shown in Figure 9c, sufficient cooling power to obtain a maximum temperature difference of less than 5 K over the battery after discharging at 3 C can be obtained by increasing the flow rate to 0.5 L/min. There, the temperature difference in plane is approximately 1 K, while the through-plane temperature difference is approximately 4 K. Thus, it is sufficient to cool only one side of the pouch cell. Nevertheless, especially for high loads cooling one or two sides of the pouch cells is a trade-off between simplified cooling system and more gentle battery operation by smaller temperature gradients.

Generally, for higher battery loads with much stronger cooling requirements, the limiting factor for homogenous cooling of pouch cells seems to be the low transversal thermal conductivity of the pouch cell. Thereby, the generated heat could not be transported fast enough from the uncooled to the cooled side of the battery. Hence, a large temperature gradient will develop through the battery, potentially exceeding the previously defined maximum temperature difference within the battery of 5 K. As further calculations show, even an increase in the cooling power, providing a low temperature on one battery-cooling plate interface, would have no significant effect on the maximum temperature difference. But vice versa if one would allow a temperature difference of 7 K over the battery, for discharging with 3 C (similar to Figure 9b), a flow rate of 0.2 L/min would be sufficient. By

allowing higher temperature gradients over the battery, the cooling system can still keep a fine average temperature.

## 5. Setup and Experimental Validation of the Water-Cooled Battery System

### 5.1. Setup of the Battery System

Based on the results of the simulated cooling plates, a complete battery module as part of a battery system is set up. The battery system includes up to twelve electrically connected battery modules. Each battery module (see Figure 10) consists of twelve serially connected pouch cells from LITARION (for details see above). A battery management system (BMS) is placed on top of the batteries. It measures relevant battery and cell data, such as current, cell and module voltage, and temperature. Hence, the BMS ensures a safe battery operation and covers all battery modules. Furthermore, the BMS sets up the communication for a battery system, comprising multiple battery modules and the power electronic converter. Details of the BMS are described by Bischof [66].

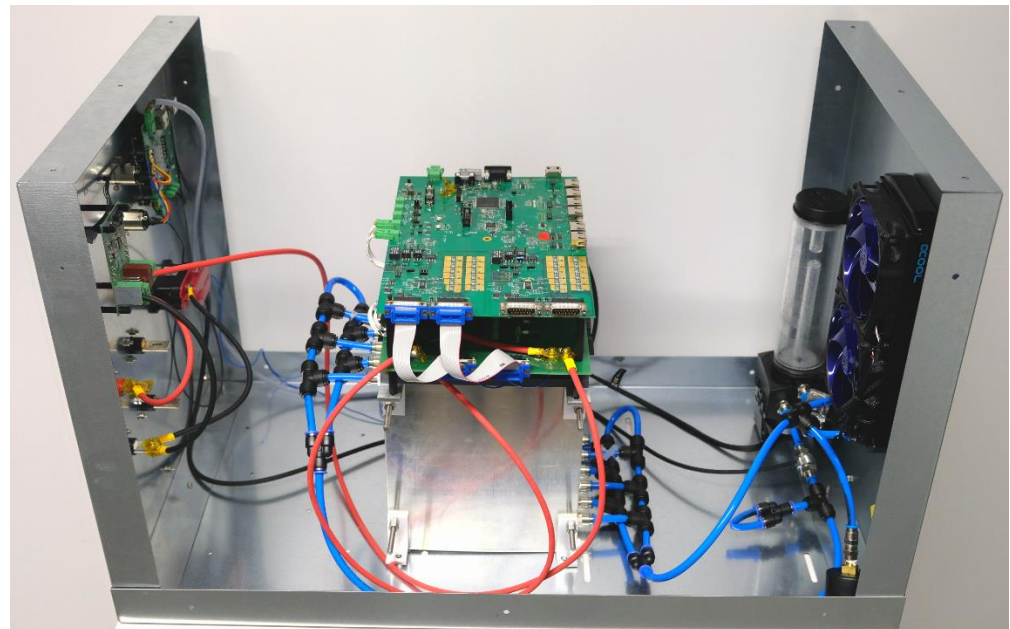


**Figure 10.** Photo of the battery module with the integrated cooling system. On top of the batteries in the middle part is the BMS placed. The power electronics is mounted directly below the BMS and on the left-hand side of the box. On the right-hand side pump, fans, and the cooling system radiator are placed.

A further task of the BMS is controlling the cooling unit, which can be seen in Figure 10 on the right-hand side. The cooling system comprises parts from commercially available water-cooling systems for computers. The fluid pump has a maximum flow rate of 5.7 L/min and the two fans based on a radiator have a maximum air flow rate of 164 m<sup>3</sup>/h each. The pump and fans are continuously varied by a pulse-width modulated (PWM) signal. In the cooling circuit, a manometer, a thermometer, and a flowmeter are integrated, providing data to the BMS to control the pumping power. The pumping and fan power define the cooling power. A simple proportional controller using the actual and desired temperature difference determines the cooling capacity. This ensures finding a steady state cooling power with continuous operation to minimize the system's and batteries' stress due to temperature changes. Furthermore, there is a maximum and minimum temperature at which cooling is deactivated or running at full power.

For the heat removal from the batteries, thin aluminum cooling plates are placed between every second battery (see Figure 11a) so that one side of each battery is cooled. Aluminum was chosen due to its low weight, good thermal conductivity, and machinability.

On top of these cooling plates are isolating plastic frames with aluminum current collectors that are mounted to connect the cells electrically. Figure 11b shows a unit of such a cooling plate with a pouch cell on both sides. A threaded rod through all the cooling plates is used to clamp the batteries between the cooling plates. A heat-conducting foil (THORA H400 Thermal Pad) with 0.5 mm thickness and 4 W/mK thermal conductivity is used to create good thermal contact between the cooling plate and the battery. Additionally, the foil compensates for small bumps at the interface.

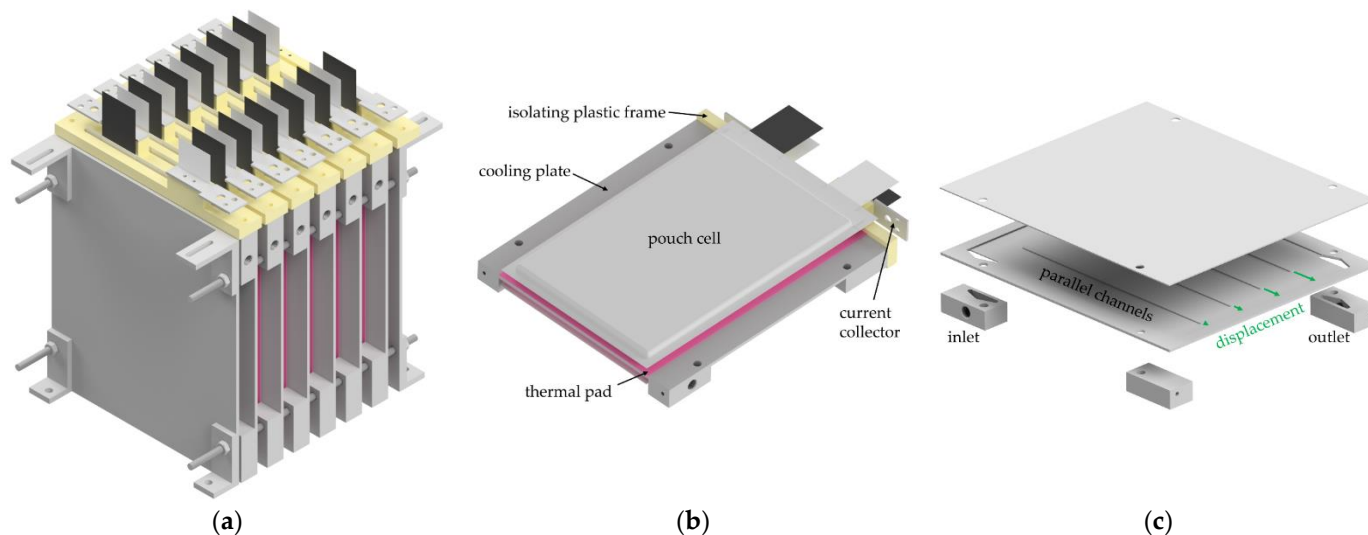


**Figure 11.** Setup of the battery block with cooling plates: (a) battery block with twelve pouch cells in between of six cooling plates. (b) Unit of a cooling plate with one pouch cell on both sides. (c) Exploded drawing of the cooling plate. Green arrows mark the different displacements of the internal walls.

The cooling plates are manufactured from a 2 mm aluminum plate on which a 1 mm thick fluid channel structure is milled. Based on the previous simulations, a design with parallel fluid channels was preferred for the internal structure. The parallel fluid channel design consists of an inlet and outlet channel on the upper and lower parts of the cooling plate. The fluid inlet and outlet themselves are placed on the upper left and lower right, respectively. Separate blocks of 15 mm high on the downside of the cooling plate connect the internal channels with an external connector (see Figure 11b). The cooling plate is divided into five parallel channels by interior walls to further guide the fluid from inlet to outlet. A displacement of the interior walls along their axis improves the homogeneity of the fluid flow through the parallel channels. As shown in Figure 11c, the displacement increases from the outlet to the inlet side.

The top of the cooling plate is sealed with a 1 mm aluminum cover plate. In the first step, this plate was glued together with the plate with the channel structure. Therefore, a structural adhesive (DELO Monopox 1197) was deposited by screen printing on the cover plate. After curing, inlet and outlet blocks were glued on the lower side of the cooling plate in a second screen printing step.

Standard 1/8" quick connectors with an appropriate hose link all parts of the cooling circuit. The cooling plates are connected in parallel to achieve an equal inlet temperature and thus homogenous cooling power of all batteries.

The total 4-mm thick cooling plate with heat-conducting foil enhances the thickness of the battery stack by 14%. However, considering the otherwise necessary gaps of at least 5 mm between the batteries for sufficient passive air cooling decreases the stack thickness and, in addition to that, the volumetric energy density by 18%. The gravimetric energy density of the stack is lowered by approximately 20%.

## 5.2. Temperature Measurement

An integrated temperature measurement system is necessary to test the cooling system's functionality. An array of temperature sensors can reveal undesired temperature differences across the pouch cell. The temperature sensors should be placed between two pouch cells or a pouch cell and a cooling plate without strongly affecting the system. This means the temperature measurement should not interrupt the heat flux and appreciably increase the thermal resistance. Moreover, the heat capacity of the temperature sensors should be as low as possible.

Platinum resistance temperature sensors (Pt1000) with a thickness of 0.9 mm were chosen for the temperature measurement, enabling high accuracy when using four-terminal sensing. An array of 56 sensors was soldered on a metal core-printed circuit board (PCB) with high thermal conductivity (see Figure 12). The spots between the Pt1000 sensors are filled with the same heat conduction foil used in the battery system. All sensors are electrically connected with three connections to the pin headers on the side of the PCB.

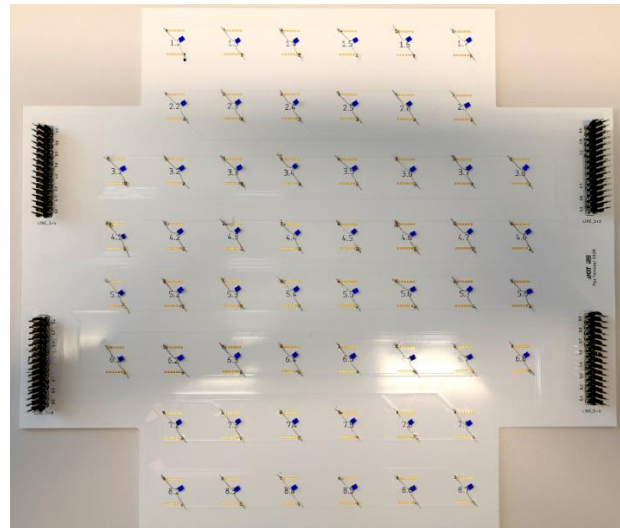


**Figure 12.** Metal core PCB with 56 soldered Pt1000 temperature sensors (blue). On the left and right, pin headers were placed to easily connect the sensors to the measurement electronics by ribbon cables.

The pin headers connect the temperature sensor array to the measurement electronics with four connections for each sensor. A multi-sensor, high-accuracy digital temperature measurement system from Linear Technology, model LTC 2983, is used for measuring the temperature sensors. This measurement chip can measure different temperature sensors, including the Pt1000. The LTC 2983 directly exports a measured voltage or resistance as a temperature value. Since the chip does not have enough input channels for all sensors, a combination of multiplexers successively selects all array sensors for readout. As shown in Figure 13, one  $8 \times 2$  analog multiplexer is used for selecting the column ( $x$ ) and another  $8 \times 2$  analog multiplexer is used for selecting the sensors' rows ( $y$ ). To correctly choose one sensor without bypassing it through the grid of sensors, for each column  $i$  an additional  $8 \times 2$  analog multiplexer ( $x_i$ ) is necessary. In case of the rows, the four-terminal sensing ends at the first sensors with negligible influence on accuracy. This simplifies the setup because no further multiplexers and corresponding connecting lines are needed for correct measurements. Due to the analog multiplexer with an on-resistance of approximately  $150 \Omega$  at an operating voltage of 20 V, four-terminal sensing is indispensable.

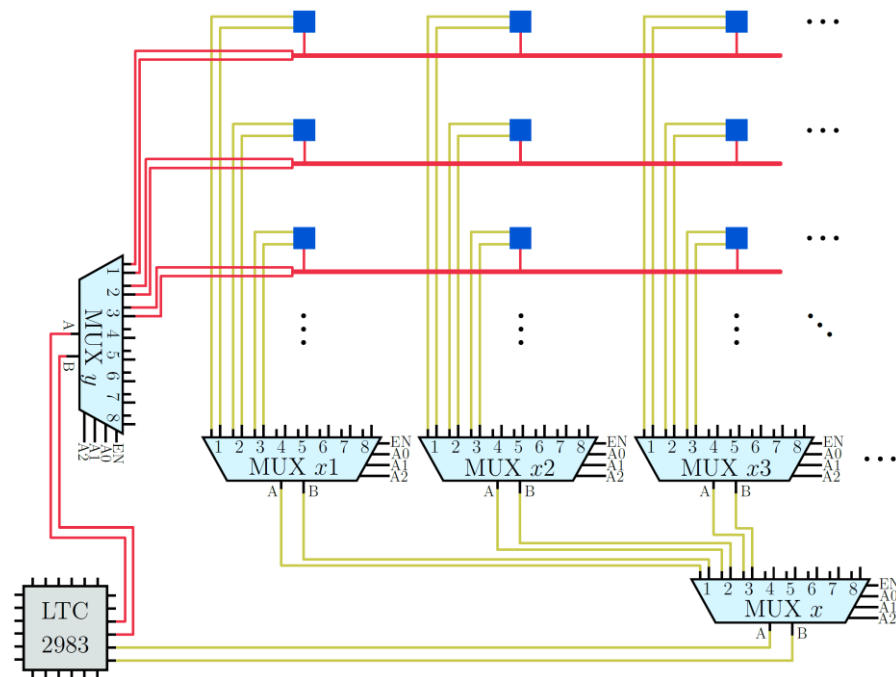


**Figure 13.** Simplified circuitry of analog multiplexers for the temperature sensor array in four-terminal sensing. To select the column ( $x$ , green) and row ( $y$ , red) of a dark blue temperature sensor, two  $8 \times 2$  multiplexers are used. For the explicit selection of one temperature sensor, each column needs an additional  $8 \times 2$  multiplexer.

The control of the multiplexer is performed with a microcontroller board (STM32 G474RE Nucleo-64). Furthermore, the microcontroller configures the settings, does the readout of the LTC2983, and transmits the data to a computer with a custom LabVIEW program processing the data. Limited by the readout time of the LTC 2983, the measurement routine takes approximately 10 s.

### 5.3. System Load Test

These temperature sensor arrays are placed in the battery pack. One array is placed between two pouch cells and another at the interface of a cooling plate and a pouch cell. To prohibit the mutual influence of the cooling plates in the system, the two plates were placed at the distance of multiple pouch cells inside the system, assuming a similar behavior of all pouch cells.

To better evaluate the effect of the cooling plates, a test of the battery pack with deactivated cooling was conducted first. After discharging the battery at  $1\text{ C}$ , a precise temperature increase of  $8\text{ K}$  was measured. Figure 14 confirms the expected temperature distribution with the hottest region at the top of the pouch cell where the current collectors are located [67]. Furthermore, a temperature gradient pointing from the middle to the outside of the pouch cell can be seen due to the reduced convective heat dissipation in the center. Since the four sensors on the left and right of the sensor array are not fully touching the pouch cell, they are strongly influenced by the environment and, hence, lower the measured temperature. Note that the temperature distribution in Figure 14 was measured between the two pouch cells. The temperature distribution at the interface of the pouch cell and the cooling plate reveals a slightly lower average temperature due to the additional thermal mass of the cooling plate. Furthermore, the temperature gradient from the top to the bottom part was lowered by the good thermal conductivity of the aluminum cooling plate.

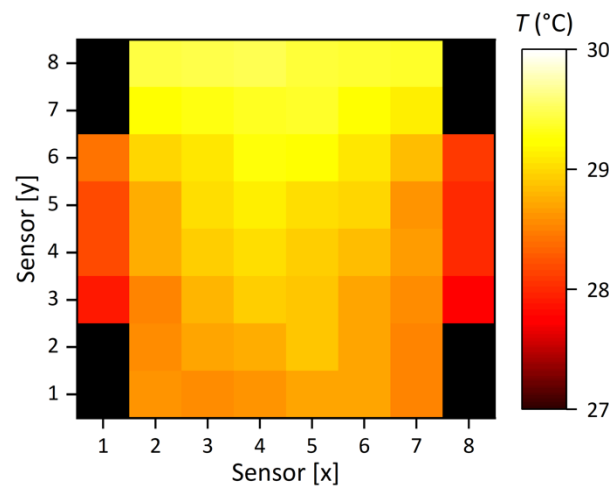


**Figure 14.** Temperature distribution inside the battery pack between two pouch cells with deactivated cooling after discharging with 1 C. At the start, the system had an environment temperature of 22 °C.

Other than lowering the average temperature of the pouch cells, the cooling plates should homogenize the natural temperature distribution shown in Figure 14. As the temperature distribution after discharging with 1 C in Figure 15 exhibits, the temperature hot spot in the top and middle region of the pouch cell is almost entirely compensated. Especially on the interface between the pouch cell and the cooling plate in Figure 15a, there are no temperature differences over the surface within the measuring accuracy. The temperature differences at the side between the two pouch cells are approximately 0.5 K and, therefore, still small.

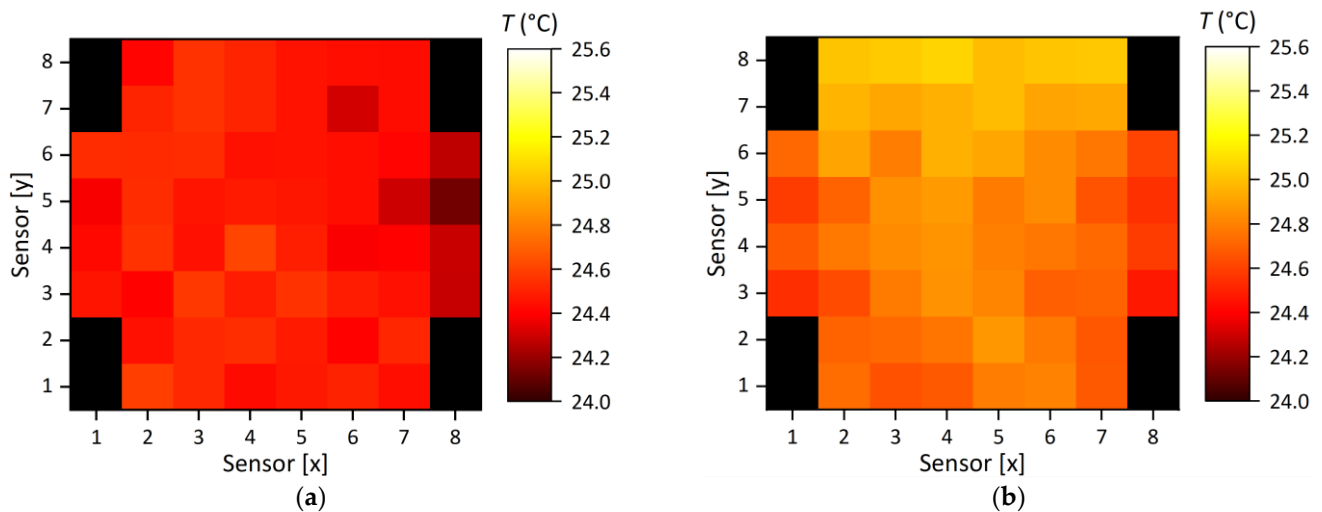


**Figure 15.** Temperature distribution after discharging with 1 C and activated cooling between (a) a pouch cell and cooling plate and (b) between two pouch cells. The water inlet is at the top left and the ambient temperature is 22 °C.

Due to the heat dissipation unit of the cooling circuit, the water inlet temperature increased compared to the ambient temperature of 22 °C by approximately 2 K.

The transversal temperature difference over the pouch cell can be depicted as the difference between Figure 15a,b, which is in good agreement with the simulation results shown in Figure 9a. A low surface averaged temperature difference of 0.6 K confirms the construction of the water-cooled battery pack and enables even higher loads with a safe and gentle operation window.

## 6. Conclusions

The lumped battery model with nondestructively determined battery parameters was successfully applied to describe a Li-ion battery electrically and hence thermally. Limitations of the lumped battery model can be seen for high and low SOC, where the model's accuracy is low, especially for high currents. Moreover, it is only possible to calculate the average heating of the battery due to the missing internal structure of the battery. Nevertheless, the model's accuracy is sufficient for a quantitative estimation of the heat generation of an operated battery to configure a cooling system further.

The simulative investigation of the developed cooling system confirms sufficient cooling of the pouch cells up to high discharge rates of 3 C. The limiting factor for higher C-rates is the pouch cells' low transversal thermal conductivity, which leads to insufficient heat transfer. In contrast to other pouch cell cooling systems [36,47,68–70], we showed that it is sufficient to cool only one side of the pouch cells under typical cycling conditions. Therefore, the battery pack contains only half of the number of cooling plates and hence is more compact and lightweight, increasing gravimetric and volumetric energy density and reducing costs.

Cooling plates composed of aluminum showed excellent cooling efficiency, while an easily scalable fabrication is possible by gluing the individual parts together. Additionally, the high thermal conductivity of aluminum cooling plates leads to a fast homogenization of inhomogeneous temperature distributions, which is typically observed for pouch cells.

An array of temperature sensors based on a metal-core PCB is introduced as a powerful tool for the experimental evaluation of the temperature distribution inside dense battery packs. A thin foil with printed temperature sensors connected to the developed measurement electronics as a promising alternative to the metal core PCB to further reduce the impact of the battery system is under research.

A comprehensive understanding is observed by comparing the experimental and simulative investigations. The internal temperature measurement shows that in the case of an uncooled battery pack, its temperature increases by 8 K after discharging at 1 C, confirming the necessity of a cooling system in a dense battery pack with negligible convective cooling. Furthermore, the temperature measurement confirmed the functionality of the cooling system and its consistency with the simulative temperature distribution.

**Author Contributions:** Conceptualization, M.F. and T.B.; methodology, M.F. and T.B.; software, M.F.; validation, M.F. and T.B.; investigation, M.F. and N.U.; resources, M.F. and T.B.; data curation, M.F.; writing—original draft preparation, M.F.; writing—review and editing, T.B. and C.Z.; supervision, T.B. All authors have read and agreed to the published version of the manuscript.

**Funding:** This research received no external funding.

**Institutional Review Board Statement:** Not applicable.

**Informed Consent Statement:** Not applicable.

**Data Availability Statement:** The data presented in this article are available on request.

**Acknowledgments:** We thank Simon Bischof for the support with the power electronics and the BMS. We further thank Benjamin Leyrer for the assembly of the cooling plates. We acknowledge the support by the KIT-Publication Fund of the Karlsruhe Institute of Technology.

**Conflicts of Interest:** The authors declare no conflict of interest.

## References

1. Eshetu, G.G.; Zhang, H.; Judez, X.; Adenusi, H.; Armand, M.; Passerini, S.; Figgemeier, E. Production of high-energy Li-ion batteries comprising silicon-containing anodes and insertion-type cathodes. *Nat. Commun.* **2021**, *12*, 5459. [[CrossRef](#)] [[PubMed](#)]
2. Shi, Q.; Zhou, J.; Ullah, S.; Yang, X.; Tokarska, K.; Trzebiecka, B.; Ta, H.Q.; Rummeli, M.H. A review of recent developments in Si/C composite materials for Li-ion batteries. *Energy Stor. Mater.* **2021**, *34*, 735–754. [[CrossRef](#)]
3. Jiang, M.; Danilov, D.L.; Eichel, R.-A.; Notten, P.H.L. A Review of Degradation Mechanisms and Recent Achievements for Ni-Rich Cathode-Based Li-Ion Batteries. *Adv. Energy Mater.* **2021**, *11*, 2103005. [[CrossRef](#)]

4. Judez, X.; Eshetu, G.G.; Li, C.; Rodriguez-Martinez, L.M.; Zhang, H.; Armand, M. Opportunities for Rechargeable Solid-State Batteries Based on Li-Intercalation Cathodes. *Joule* **2018**, *2*, 2208–2224. [[CrossRef](#)]
5. Yang, L.; Deng, W.; Xu, W.; Tian, Y.; Wang, A.; Wang, B.; Zou, G.; Hou, H.; Deng, W.; Ji, X. Olivine  $\text{LiMn}_x\text{Fe}_{1-x}\text{PO}_4$  cathode materials for lithium ion batteries: Restricted factors of rate performances. *J. Mater. Chem. A* **2021**, *9*, 14214–14232. [[CrossRef](#)]
6. Choi, D.; Shamim, N.; Crawford, A.; Huang, Q.; Vartanian, C.K.; Viswanathan, V.V.; Paiss, M.D.; Alam, M.J.E.; Reed, D.M.; Sprenkle, V.L. Li-ion battery technology for grid application. *J. Power Sources* **2021**, *511*, 230419. [[CrossRef](#)]
7. Masias, A.; Marcicki, J.; Paxton, W.A. Opportunities and Challenges of Lithium Ion Batteries in Automotive Applications. *ACS Energy Lett.* **2021**, *6*, 621–630. [[CrossRef](#)]
8. Gandoman, F.H.; Behi, H.; Berecibar, M.; Jaguemont, J.; Aleem, S.H.A.; Behi, M.; van Mierlo, J. Reliability evaluation of Li-ion batteries for electric vehicles applications from the thermal perspectives. In *Uncertainties in Modern Power Systems*; Elsevier: Amsterdam, The Netherlands, 2021; pp. 563–587. ISBN 9780128204917.
9. Nitta, N.; Wu, F.; Lee, J.T.; Yushin, G. Li-ion battery materials: Present and future. *Mater. Today* **2015**, *18*, 252–264. [[CrossRef](#)]
10. European Commission. *Joint Research Centre. Li-Ion Batteries for Mobility and Stationary Storage Applications: Scenarios for Costs and Market Growth*; Publications Office: Petten, The Netherlands, 2018.
11. Saez-de-Ibarra, A.; Martinez-Laserna, E.; Stroe, D.-I.; Swierczynski, M.; Rodriguez, P. Sizing Study of Second Life Li-ion Batteries for Enhancing Renewable Energy Grid Integration. *IEEE Trans. Ind. Appl.* **2016**, *52*, 4999–5008. [[CrossRef](#)]
12. Birkl, C.R.; Frost, D.F.; Bizeray, A.M.; Richardson, R.R.; Howey, D.A. Modular converter system for low-cost off-grid energy storage using second life li-ion batteries. In Proceedings of the 2014 IEEE Global Humanitarian Technology Conference (GHTC 2014), San Jose, CA, USA, 10–13 October 2014; IEEE: Piscataway, NJ, USA, 2014; pp. 192–199, ISBN 978-1-4799-7193-0.
13. Diouf, B.; Pode, R. Potential of lithium-ion batteries in renewable energy. *J. Renew. Energy* **2015**, *76*, 375–380. [[CrossRef](#)]
14. Waldmann, T.; Quinn, J.B.; Richter, K.; Kasper, M.; Tost, A.; Klein, A.; Wohlfahrt-Mehrens, M. Electrochemical, Post-Mortem, and ARC Analysis of Li-Ion Cell Safety in Second-Life Applications. *J. Electrochem. Soc.* **2017**, *164*, A3154–A3162. [[CrossRef](#)]
15. Chen, Y.; Kang, Y.; Zhao, Y.; Wang, L.; Liu, J.; Li, Y.; Liang, Z.; He, X.; Li, X.; Tavajohi, N.; et al. A review of lithium-ion battery safety concerns: The issues, strategies, and testing standards. *J. Energy Chem.* **2021**, *59*, 83–99. [[CrossRef](#)]
16. Al-Zareer, M.; Dincer, I.; Rosen, M.A. A review of novel thermal management systems for batteries. *Int. J. Energy Res.* **2018**, *42*, 3182–3205. [[CrossRef](#)]
17. Raj, A.; Rodrigues, M.-T.F.; Abraham, D.P. Rate-Dependent Aging Resulting from Fast Charging of Li-Ion Cells. *J. Electrochem. Soc.* **2020**, *167*, 120517. [[CrossRef](#)]
18. Preger, Y.; Barkholtz, H.M.; Fresquez, A.; Campbell, D.L.; Juba, B.W.; Romàn-Kustas, J.; Ferreira, S.R.; Chalamala, B. Degradation of Commercial Lithium-Ion Cells as a Function of Chemistry and Cycling Conditions. *J. Electrochem. Soc.* **2020**, *167*, 120532. [[CrossRef](#)]
19. Golubkov, A.W.; Fuchs, D.; Wagner, J.; Wiltsche, H.; Stangl, C.; Fauler, G.; Voitic, G.; Thaler, A.; Hacker, V. Thermal-runaway experiments on consumer Li-ion batteries with metal-oxide and olivin-type cathodes. *RSC Adv.* **2014**, *4*, 3633–3642. [[CrossRef](#)]
20. Aichberger, C.; Jungmeier, G. Environmental Life Cycle Impacts of Automotive Batteries Based on a Literature Review. *Energies* **2020**, *13*, 6345. [[CrossRef](#)]
21. Ecker, M.; Nieto, N.; Käbitz, S.; Schmalstieg, J.; Blanke, H.; Warnecke, A.; Sauer, D.U. Calendar and cycle life study of Li(NiMnCo)O<sub>2</sub>-based 18650 lithium-ion batteries. *J. Power Sources* **2014**, *248*, 839–851. [[CrossRef](#)]
22. Waldmann, T.; Wilka, M.; Kasper, M.; Fleischhammer, M.; Wohlfahrt-Mehrens, M. Temperature dependent ageing mechanisms in Lithium-ion batteries—A Post-Mortem study. *J. Power Sources* **2014**, *262*, 129–135. [[CrossRef](#)]
23. Bozorgchenani, M.; Kucinskis, G.; Wohlfahrt-Mehrens, M.; Waldmann, T. Experimental Confirmation of C-Rate Dependent Minima Shifts in Arrhenius Plots of Li-Ion Battery Aging. *J. Electrochem. Soc.* **2022**, *169*, 30509. [[CrossRef](#)]
24. Ma, S.; Jiang, M.; Tao, P.; Song, C.; Wu, J.; Wang, J.; Deng, T.; Shang, W. Temperature effect and thermal impact in lithium-ion batteries: A review. *Prog. Nat. Sci. Mater.* **2018**, *28*, 653–666. [[CrossRef](#)]
25. You, L.; Duan, K.; Zhang, G.; Song, W.; Yang, T.; Song, X.; Wang, S.; Liu, J. N,N-Dimethylformamide Electrolyte Additive Via a Blocking Strategy Enables High-Performance Lithium-Ion Battery under High Temperature. *J. Phys. Chem. C* **2019**, *123*, 5942–5950. [[CrossRef](#)]
26. Zhao, H.; Yu, X.; Li, J.; Li, B.; Shao, H.; Li, L.; Deng, Y. Film-forming electrolyte additives for rechargeable lithium-ion batteries: Progress and outlook. *J. Mater. Chem. A* **2019**, *7*, 8700–8722. [[CrossRef](#)]
27. Xia, J.; Ma, L.; Dahn, J.R. Improving the long-term cycling performance of lithium-ion batteries at elevated temperature with electrolyte additives. *J. Power Sources* **2015**, *287*, 377–385. [[CrossRef](#)]
28. Eom, J.-Y.; Jung, I.-H.; Lee, J.-H. Effects of vinylene carbonate on high temperature storage of high voltage Li-ion batteries. *J. Power Sources* **2011**, *196*, 9810–9814. [[CrossRef](#)]
29. Kang, K.S.; Choi, S.; Song, J.; Woo, S.-G.; Jo, Y.N.; Choi, J.; Yim, T.; Yu, J.-S.; Kim, Y.-J. Effect of additives on electrochemical performance of lithium nickel cobalt manganese oxide at high temperature. *J. Power Sources* **2014**, *253*, 48–54. [[CrossRef](#)]
30. Chang, W.J.; Kim, S.H.; Hwang, J.; Chang, J.; Yang, D.W.; Kwon, S.S.; Kim, J.T.; Lee, W.W.; Lee, J.H.; Park, H.; et al. Controlling electric potential to inhibit solid-electrolyte interphase formation on nanowire anodes for ultrafast lithium-ion batteries. *Nat. Commun.* **2018**, *9*, 3461. [[CrossRef](#)]
31. Werner, D.; Paarmann, S.; Wiebelt, A.; Wetzel, T. Inhomogeneous Temperature Distribution Affecting the Cyclic Aging of Li-Ion Cells. Part I: Experimental Investigation. *Batteries* **2020**, *6*, 13. [[CrossRef](#)]

32. Park, S.; Jung, D. Battery cell arrangement and heat transfer fluid effects on the parasitic power consumption and the cell temperature distribution in a hybrid electric vehicle. *J. Power Sources* **2013**, *227*, 191–198. [[CrossRef](#)]
33. Pesaran, A.; Vlahinos, A.; Burch, S. Thermal Performance of EV and HEV Battery Modules and Packs. In Proceedings of the 14th International Electric Vehicle Symposium, Orlando, FL, USA, 15–17 December 1997.
34. Zolot, M.; Pesaran, A.A.; Mihalic, M. Thermal Evaluation of Toyota Prius Battery Pack. In *SAE Technical Paper Series; Future Car Congress*, JUN. 03, 2002; SAE International: 400 Commonwealth Drive, Warrendale, PA, USA, 2002.
35. Wang, Y.; Gao, Q.; Wang, G.; Lu, P.; Zhao, M.; Bao, W. A review on research status and key technologies of battery thermal management and its enhanced safety. *Int. J. Energy Res.* **2018**, *42*, 4008–4033. [[CrossRef](#)]
36. Chen, D.; Jiang, J.; Kim, G.-H.; Yang, C.; Pesaran, A. Comparison of different cooling methods for lithium ion battery cells. *Appl. Therm. Eng.* **2016**, *94*, 846–854. [[CrossRef](#)]
37. Tran, T.-H.; Harmand, S.; Desmet, B.; Filangi, S. Experimental investigation on the feasibility of heat pipe cooling for HEV/EV lithium-ion battery. *Appl. Therm. Eng.* **2014**, *63*, 551–558. [[CrossRef](#)]
38. Rao, Z.; Huo, Y.; Liu, X. Experimental study of an OHP-cooled thermal management system for electric vehicle power battery. *Exp. Therm. Fluid Sci.* **2014**, *57*, 20–26. [[CrossRef](#)]
39. Al-Zareer, M.; Dincer, I.; Rosen, M.A. Novel thermal management system using boiling cooling for high-powered lithium-ion battery packs for hybrid electric vehicles. *J. Power Sources* **2017**, *363*, 291–303. [[CrossRef](#)]
40. Kizilel, R.; Sabbah, R.; Selman, J.R.; Al-Hallaj, S. An alternative cooling system to enhance the safety of Li-ion battery packs. *J. Power Sources* **2009**, *194*, 1105–1112. [[CrossRef](#)]
41. Sabbah, R.; Kizilel, R.; Selman, J.R.; Al-Hallaj, S. Active (air-cooled) vs. passive (phase change material) thermal management of high power lithium-ion packs: Limitation of temperature rise and uniformity of temperature distribution. *J. Power Sources* **2008**, *182*, 630–638. [[CrossRef](#)]
42. Wilke, S.; Schweitzer, B.; Khateeb, S.; Al-Hallaj, S. Preventing thermal runaway propagation in lithium ion battery packs using a phase change composite material: An experimental study. *J. Power Sources* **2017**, *340*, 51–59. [[CrossRef](#)]
43. Jarrett, A.; Kim, I.Y. Design optimization of electric vehicle battery cooling plates for thermal performance. *J. Power Sources* **2011**, *196*, 10359–10368. [[CrossRef](#)]
44. Lan, C.; Xu, J.; Qiao, Y.; Ma, Y. Thermal management for high power lithium-ion battery by minichannel aluminum tubes. *Appl. Therm. Eng.* **2016**, *101*, 284–292. [[CrossRef](#)]
45. Shang, Z.; Qi, H.; Liu, X.; Ouyang, C.; Wang, Y. Structural optimization of lithium-ion battery for improving thermal performance based on a liquid cooling system. *Int. J. Heat Mass Transf.* **2019**, *130*, 33–41. [[CrossRef](#)]
46. Jarrett, A.; Kim, I.Y. Influence of operating conditions on the optimum design of electric vehicle battery cooling plates. *J. Power Sources* **2014**, *245*, 644–655. [[CrossRef](#)]
47. Patil, M.; Panchal, S.; Kim, N.; Lee, M.-Y. Cooling Performance Characteristics of 20 Ah Lithium-Ion Pouch Cell with Cold Plates along Both Surfaces. *Energies* **2018**, *11*, 2550. [[CrossRef](#)]
48. Shaaia, R.; Brisbane, R.M. Battery Cell Cooling. Plate. Patent US20160043454A1, 7 August 2014.
49. Obasih, K.; Mack, R.J.; Houchin-Miller, G.P.; Dekeuster, R.M.; Fuhr, J.D. Battery System Having an External Thermal Management System. Patent EP2697860B1, 12 April 2012.
50. Maguire, P.D.; Burrows, N.R. Extended Battery Cooling. Fin. Patent US9509018B2, 16 January 2014.
51. Götz, S.; Jaensch, M.; Leidig, P. Battery. Module. Patent DE102018100394A1, 1 October 2018.
52. Newman, J.; Tiedemann, W. Porous-electrode theory with battery applications. *AIChE J.* **1975**, *21*, 25–41. [[CrossRef](#)]
53. Doyle, M.; Newman, J. The use of mathematical modeling in the design of lithium/polymer battery systems. *Electrochim. Acta* **1995**, *40*, 2191–2196. [[CrossRef](#)]
54. Bandhauer, T.M.; Garimella, S.; Fuller, T.F. Temperature-dependent electrochemical heat generation in a commercial lithium-ion battery. *J. Power Sources* **2014**, *247*, 618–628. [[CrossRef](#)]
55. Ekström, H.; Fridholm, B.; Lindbergh, G. Comparison of lumped diffusion models for voltage prediction of a lithium-ion battery cell during dynamic loads. *J. Power Sources* **2018**, *402*, 296–300. [[CrossRef](#)]
56. COMSOL AB. *COMSOL Multiphysics*; COMSOL AB: Stockholm, Sweden, 2019.
57. Petzl, M.; Danzer, M.A. Advancements in OCV Measurement and Analysis for Lithium-Ion Batteries. *IEEE Trans. Energy Convers.* **2013**, *28*, 675–681. [[CrossRef](#)]
58. Baronti, F.; Zamboni, W.; Roncella, R.; Saletti, R.; Spagnuolo, G. Open-circuit voltage measurement of Lithium-Iron-Phosphate batteries. In Proceedings of the 2015 IEEE International Instrumentation and Measurement Technology Conference (I2MTC), Pisa, Italy, 11–14 May 2015; IEEE: New York, NY, USA, 2015; pp. 1711–1716, ISBN 978-1-4799-6114-6.
59. Plett, G. *Battery Management Systems, Volume I*; Artech House: Norwood, MA, USA, 2015; ISBN 978-1-63081-023-8.
60. Fan, G.; Pan, K.; Canova, M.; Marcicki, J.; Yang, X.G. Modeling of Li-Ion Cells for Fast Simulation of High C-Rate and Low Temperature Operations. *J. Electrochem. Soc.* **2016**, *163*, A666–A676. [[CrossRef](#)]
61. Marcicki, J.; Yang, X.G. Model-Based Estimation of Reversible Heat Generation in Lithium-Ion Cells. *J. Electrochem. Soc.* **2014**, *161*, A1794–A1800. [[CrossRef](#)]
62. Korthauer, R. *Handbuch Lithium-Ionen-Batterien*; Springer Berlin Heidelberg: Berlin/Heidelberg, Germany, 2013; ISBN 978-3-642-30652-5.

63. Maleki, H.; Wang, H.; Porter, W.; Hallmark, J. Li-Ion polymer cells thermal property changes as a function of cycle-life. *J. Power Sources* **2014**, *263*, 223–230. [[CrossRef](#)]
64. Chen, M.; Bai, F.; Song, W.; Lv, J.; Lin, S.; Feng, Z.; Li, Y.; Ding, Y. A multilayer electro-thermal model of pouch battery during normal discharge and internal short circuit process. *Appl. Therm. Eng.* **2017**, *120*, 506–516. [[CrossRef](#)]
65. Viswanathan, V.V.; Choi, D.; Wang, D.; Xu, W.; Towne, S.; Williford, R.E.; Zhang, J.-G.; Liu, J.; Yang, Z. Effect of entropy change of lithium intercalation in cathodes and anodes on Li-ion battery thermal management. *J. Power Sources* **2010**, *195*, 3720–3729. [[CrossRef](#)]
66. Bischof, S. Rekonfigurierbare Lithium-Ionen-Batterien für den Betrieb von Industriellen Produktionsstätten. Ph.D. Thesis, KIT, Karlsruhe, Germany, 2020.
67. Goutam, S.; Nikolian, A.; Jaguemont, J.; Smekens, J.; Omar, N.; van Dan Bossche, P.; van Mierlo, J. Three-dimensional electro-thermal model of li-ion pouch cell: Analysis and comparison of cell design factors and model assumptions. *Appl. Therm. Eng.* **2017**, *126*, 796–808. [[CrossRef](#)]
68. Zhang, T.; Gao, Q.; Wang, G.; Gu, Y.; Wang, Y.; Bao, W.; Zhang, D. Investigation on the promotion of temperature uniformity for the designed battery pack with liquid flow in cooling process. *Appl. Therm. Eng.* **2017**, *116*, 655–662. [[CrossRef](#)]
69. Bai, F.; Chen, M.; Song, W.; Feng, Z.; Li, Y.; Ding, Y. Thermal management performances of PCM/water cooling-plate using for lithium-ion battery module based on non-uniform internal heat source. *Appl. Therm. Eng.* **2017**, *126*, 17–27. [[CrossRef](#)]
70. Huo, Y.; Rao, Z.; Liu, X.; Zhao, J. Investigation of power battery thermal management by using mini-channel cold plate. *Energy Convers. Manag.* **2015**, *89*, 387–395. [[CrossRef](#)]